Direct Numerical Simulation of Energy Separation Effect in the Near Wake behind a Circular Cylinder

Andrey I. Aleksyuk[a,b,*], Alexander N. Osiptsov[c]

[a]*Faculty of Mechanics and Mathematics, Lomonosov Moscow State University, Moscow 119991, Russian Federation*
[b]*Water Problems Institute, Russian Academy of Sciences, Moscow 119333, Russian Federation*
[c]*Institute of Mechanics, Lomonosov Moscow State University, Moscow 119192, Russian Federation*

Abstract

Based on direct numerical simulation of two-dimensional Navier–Stokes equations, the effect of energy separation in unsteady vortex flows is investigated with the reference to the problem of a compressible viscous flow past a thermally insulated circular cylinder. The range of Reynolds ($\mathrm{Re} \leq 10^3$), Prandtl ($0.1 \leq \mathrm{Pr} \leq 10$) and Mach ($\mathrm{M} \leq 0.6$) numbers considered corresponds mainly to the periodic vortex shedding regime. The energy separation, associated with the vortex shedding process, manifests itself in the appearance of cold and hot (in terms of total temperature) spots in the near wake. The main attention is focused on the comparative analysis of different mechanisms of total-enthalpy variation in a fluid particle moving around the cylinder, such as the action of viscosity, thermal conductivity, and unsteadiness of the flow. It is shown that the time-averaged total-enthalpy stratification in the boundary layer is caused by dissipative mechanisms. In the vortex formation region and in the vortex street, a decrease in the time-averaged total enthalpy is attributable mainly to the streamline oscillations. The known Eckert–Weise effect of low equilibrium temperature at the rearmost stagnation point of the cylinder is associated with the non-uniformities in the temperature and density fields, created by the evolution of recirculation zones near the body surface. For both instantaneous and time-averaged flow patterns, the regions of local increase and decrease in the total enthalpy are distinguished. It turned out that, in the time-averaged flow, the region responsible for the total-enthalpy decrease in the vortex formation zone does not affect the decrease in the total enthalpy in the developed vortex wake, and vice versa.

Keywords: energy separation, total enthalpy, unsteady vortex flows, near wake, boundary layer, time-averaged flow, thermally insulated cylinder, Navier–Stokes equations

1. Introduction

The interest in the process of energy separation in compressible gas flows is associated with the practical need for devices capable of separating a gas flow into cold and hot streams (with low and high total temperatures) without mechanical work or external heat supply. For the first time, such a device was proposed in the early 1930-s by G. Ranque and was called a vortex tube (Ranque–Hilsch vortex tube) [1]. A review of later research on Ranque–Hilsch vortex tubes can be found in [2]. A Ranque–Hilsch vortex tube may ensure an appreciable difference in the stagnation temperatures of the outlet cold and hot streams but has a serious disadvantage associated with too high losses of the total pressure. An alternative scheme of machine-free energy separation, the so-called Leontiev tube [3, 4], is devoid of this disadvantage but ensures much smaller efficiency of energy separation. This scheme is based on heat transfer between high-speed (usually supersonic) and low-speed (subsonic) streams having identical stagnation parameters and separated by a thin wall with a low thermal resistance. At present, different methods of enhancing the efficiency of scheme [3] are under study. Among them are: the use of a perforated partition wall, a slot or distributed gas injection or suction on the wall, the creation of a relief on the wall, addition of an admixture of small droplets evaporating in the supersonic boundary layer [5], etc. The main aim of all these methods is to reduce the recovery temperature in the high-speed boundary layer, which then may result in an increase in the heat fluxes through the partition wall and enhancement of energy separation.

In this regard, of substantial interest is the well-known Eckert–Weise effect of low recovery temperature on the rear part of the surface of a thermally insulated cylinder immersed in a compressible gas flow, detected experimentally in the early 1940-ies [6].

The Eckert–Weise effect is commonly associated with a non-stationary vortex shedding process. This connection was suggested by L.F. Ryan [7] and since then has been studied in a number of works, most of which were experimental (see, for instance, [7–14]). In an extensive study [9], the authors showed that the intensification of the vor-

*Corresponding author.
Email addresses:* aleksyuk@mech.math.msu.su (Andrey I. Aleksyuk), osiptsov@imec.msu.ru (Alexander N. Osiptsov)

Nomenclature

M	Mach number
$\mathcal{P}, \mathcal{A}, \mathcal{Q}$	contributions of non-stationarity, viscous forces, and thermal conductivity in total-enthalpy variation rate
Pr	Prandtl number
Re	Reynolds number
St	Strouhal number
$\boldsymbol{n}$	unit normal vector
$\boldsymbol{u}$	velocity vector (u, v)
$\boldsymbol{x}$	vector of Cartesian coordinates (x, y)
C_D	drag coefficient
C_L	lift coefficient
c_V, c_p	specific heats at constant volume and pressure
d	cylinder diameter
E	efficiency of energy separation
e	internal energy
f	vortex shedding frequency
I_0	normalized total enthalpy
i_0	total enthalpy
p	pressure
R	distance from the cylinder surface
T	temperature
t	time

U	magnitude of the velocity vector
X_{in}, X_{out}, Y	distance from the center of the cylinder to the inlet, outlet, and side boundaries of the corresponding subdomains
α	polar angle in clockwise direction, measured from the frontal stagnation point
Δ	approximate size of triangular elements of mesh
δ, δ_T	thicknesses of dynamic and thermal boundary layers
γ	specific-heat ratio
κ	thermal conduction coefficient
μ	viscosity coefficient
ρ	density
$\boldsymbol{\tau}$	viscous stress tensor
ε	energy
$\boldsymbol{\omega}$	vorticity vector
$(\cdot)_{,i}$	coordinate derivatives, $i = 1, 2$ corresponds to x, y
$(\cdot)_{,t}$	time derivatives
0	stagnation (or total) parameters
∞	free-stream parameters
$'$	dimensional parameters
$*$	transposition
$\overline{(\cdot)}$	time-averaged value

tex street (attained by producing acoustic waves in a wind tunnel) decreases the recovery factor at the rearmost point of the cylinder, and based on some numerical calculations they suggested a theoretical explanation of energy redistribution in the vortex street.

The time-averaged flow in the central part of the wake turns out to be cooled and have the total temperature considerably smaller than that in the free stream. With increase in the distance from the body, this effect is being weakened [13]. At the same time, as shown numerically in [9], instantaneous total-temperature distributions contain also fairly well-marked hot spots, which are almost eliminated in the time-averaged patterns [9, 13]. The presence of hot spots behind a circular cylinder was also detected in the time-resolved experimental measurements of total temperature [11, 14]. The consideration of idealized fluid-particle trajectories and the motion of low pressure regions inside the vortices makes it possible to suggest a simple explanation of the formation of nonuniformities

in the time-averaged and instantaneous total-temperature patterns [9]. The key mechanism of the total-enthalpy variation is associated with pressure fluctuations at fixed points of space. In Section 3.1.2, this statement will be confirmed by considering individual fluid-particle trajectories in a vortex street and calculating the total enthalpy using direct numerical simulation.

However, the simple explanation of energy separation in a developed vortex street and the experimentally confirmed connection between the vortex street intensity and the recovery temperature at the rearmost point do not provide a complete explanation of the Eckert–Weise effect. Between these two phenomena (energy separation in the vortex street and the Eckert–Weise effect), there lies the process of vortex formation, which is more complex than the flow in the vortex street, and hence all dissipative mechanisms need to be considered. In Section 3.2, we show that the time-averaged wake can be divided into two subregions with different reasons for cooling: a subregion

2

of a developed vortex street and a subregion of vortex formation. The coldest region turns out to be located in the rear part of the cylinder, where the vortices are formed. To clarify the underlying physics of the effect of decrease in the total temperature in the near wake, including the vortex formation region, is the main aim of our study, which is likely to make it possible to use this effect for improving the efficiency of energy separation devices.

We also aim at giving the quantitative comparison of the contribution of different mechanisms to the energy separation in the near wake on the basis of direct numerical simulation of compressible viscous flow around a cylinder. From the equation of total-enthalpy variation in a fluid particle, it follows that energy separation can be caused by three mechanisms [10]: non-stationarity of the flow (pressure variations at fixed locations), the thermal-conduction effect, and the work of the viscous forces. As will be shown below (Section 3.2), in the time-averaged equation for the total enthalpy a new term (mechanism), associated with the time averaged convective derivative, appears. We will analyze the role of different mechanisms in the energy separation effect for both instantaneous and time-averaged flow fields over a fairly wide range of Reynolds ($30 \leq \mathrm{Re} \leq 10^3$), Mach ($0.1 \leq \mathrm{M} \leq 0.6$), and Prandtl ($0.1 \leq \mathrm{Pr} \leq 10$) numbers.

Our study is based on direct numerical solution of the Navier–Stokes equations obtained with a controlled accuracy by the Galerkin least-squares (GLS) finite-element method on unstructured triangular meshes (Section 2). The results (Section 3) are divided into two parts. In Section 3.1, we discuss the reasons for the variation of the total enthalpy in fluid particles in both the laminar boundary layer and the vortex wake. Section 3.2 is devoted to the study of energy separation in the time-averaged flow. The time-averaged equation of total-enthalpy variation is written in two different forms, and the physical meaning and contribution of different terms (mechanisms) in these equations to the energy separation are studied. In Section 3.2, a time-averaged flow scheme is given, which shows the localization of typical regions of decrease in total enthalpy. The influence of the Reynolds, Mach, and Prandtl numbers on the efficiency of energy separation is discussed in Section 3.2.3.

2. Problem Formulation and Numerical Method

The two-dimensional problem of a crossflow of a viscous compressible gas past a circular cylinder is considered in the Cartesian coordinate system (x, y), with the origin located at the center of the cylinder. The model of a perfect viscous gas with constant specific heats, viscosity, and thermal conductivity is used. The Navier–Stokes equations governing the fluid flow in primitive variables $Y(x, t) = (p, u, v, T)^*$ ($*$ signifies transposition) can be written as follows:

$$A_0 Y_{,t} + A_i Y_{,i} = \left(K_{ij} Y_{,j} - P_i \right)_{,i}. \tag{1}$$

The unknown functions of time t and coordinates $x = (x, y)$ are the dimensionless pressure $p(x, t)$, velocity $u(x, t) = (u, v)$, and temperature $T(x, t)$. Matrices A_0, A_i, K_{ij} and vector P_i ($i, j = 1, 2$) arise due to the transition from the conservative variables to the primitive 'pressure-velocity-temperature' variables (the explicit expressions are given in Appendix A). In Eq. (1), the repeated indices imply summation, and the short notation for the derivatives is used $(\cdot)_{,t} = \partial(\cdot)/\partial t$, $(\cdot)_{,1} = \partial(\cdot)/\partial x$, $(\cdot)_{,2} = \partial(\cdot)/\partial y$. All quantities are dimensionless, nondimensionalization is performed using the following formulas (here, dimensional quantities are denoted by primes)

$$t = \frac{U_\infty t'}{d}, \ x = \frac{x'}{d}, \ p = \frac{p'}{\rho_\infty U_\infty^2}, \ u = \frac{u'}{U_\infty}, \ T = \frac{c_V T'}{U_\infty^2}, \ \rho = \frac{\rho'}{\rho_\infty},$$

The Reynolds Re, Prandtl Pr, Mach M, and Strouhal St numbers are given by the formulas:

$$\mathrm{Re} = \frac{\rho_\infty U_\infty d}{\mu}, \ \mathrm{Pr} = \frac{\mu c_p}{\kappa}, \ \mathrm{M} = \frac{U_\infty}{c_\infty}, \ \mathrm{St} = \frac{fd}{U_\infty}.$$

Here, d is the diameter of the cylinder; ρ_∞, p_∞, U_∞ are the free-stream density, pressure, and velocity; κ, μ are the thermal conduction and viscosity coefficients; c_V, c_p are the specific heats at constant volume and pressure; $c_\infty = \sqrt{\gamma p_\infty/\rho_\infty}$ is the sonic velocity in the free stream; $\gamma = 1.4$ is the specific heat ratio; and f is a characteristic vortex shedding frequency.

At infinity, the flow is assumed to be uniform and directed along the x axis $u = (1, 0)$, the pressure $p = 1/(\gamma \mathrm{M}^2)$, and the temperature $T = 1/[\gamma(\gamma - 1)\mathrm{M}^2]$. On the cylinder surface, the velocity no-slip $u = (0, 0)$ and adiabatic-wall (zero heat flux) $\nabla T \cdot n = 0$ conditions are prescribed (here, n is a unit normal vector).

The problem is solved by the Galerkin least-squares (GLS) finite-element method on unstructured triangular meshes. In this method, an additional term in the least-squares form is introduced in the standard Galerkin variational equation to improve the stability of the numerical method. The original problem is reduced to a system of nonlinear algebraic equations, which is solved by Newton's iterative method with the generalized minimum-residual algorithm (GMRES). More details on the use of the present numerical approach and a review on the stabilized finite-element methods for compressible flows can be found in [15–18].

It should be noted that, for most regimes considered below, the real flow behind the cylinder is three-dimensional and turbulent. In addition, it could be necessary to take into account the dependence of the viscosity and thermal conduction coefficients on temperature. Nevertheless, we believe that our problem formulation makes it possible to understand the underlying physics and to distinguish the basic mechanisms of energy separation in the flow considered.

Domain	Δ	X_{in}	X_{out}	Y
Boundary layer	0.0005	-	-	-
Near wake	0.025	1.5	11	2
Middle wake	0.05	5	50	7.5
Far wake	0.25	10	100	15
Entire domain	2.5	200	400	200

Table 1: Parameters of the main mesh, number of nodes and elements are $N_v = 720418$, $N_e = 1440836$. Δ is the approximate size of triangular elements of the mesh, X_{in}, X_{out}, Y are the distances from the center of the cylinder to the inlet, outlet, and side boundaries of the corresponding subdomains.

2.1. Testing of the algorithm

Table 1 contains the values of mesh parameters used in all calculations below. The dimensions of the computational domain are sufficiently large (400×600), which makes it possible to reduce the possible influence of boundary conditions on the artificial boundary 'at infinity'. To improve the efficiency of the calculations, the computational domain is divided into several nested subdomains with different step sizes. In the region of interest (the near wake), we have a high-resolution mesh, while further downstream the mesh resolution decreases.

We consider the regimes with $100 \leqslant \mathrm{Re} \leqslant 10^3$, $0.1 \leqslant \mathrm{Pr} \leqslant 10$, $0.1 \leqslant \mathrm{M} \leqslant 0.6$, which gives us the following minimal estimate (at $\mathrm{Re} = 10^3$ and $\mathrm{Pr} = 10$) of the thicknesses of dynamic δ and thermal δ_T boundary layers:

$$\delta \sim \frac{1}{\sqrt{\mathrm{Re}}} \approx 0.032, \quad \delta_T \sim \frac{1}{\sqrt{\mathrm{PrRe}}} \approx 0.01.$$

That is why in this case we have approximately 20 nodes in the transverse direction for the thermal boundary layer and 60 nodes for the dynamic boundary layer.

The influence of the variation of the mesh size and the time step Δt is investigated for the extreme case $\mathrm{Re} = 10^3$, $\mathrm{M} = 0.4$, $\mathrm{Pr} = 10$. We did not consider the regime with $\mathrm{M} = 0.6$ for these purposes because in this case the flow becomes transonic, non-periodic, and the solution of the initial-boundary value problem is more sensitive to the perturbations of the numerical method. Accordingly, the comparison of the results on different meshes becomes much more complicated. For $\Delta t = 0.005$, the calculated mean value of the drag coefficient $\overline{C_D} = 1.731$, the amplitude of the lift coefficient $\Delta C_L = 1.565$, and the Strouhal number $\mathrm{St} = 0.24$. The five-fold decrease in Δt results in a variation of each of these values by less than 0.2%. The two-fold reduction of the mesh spacing changes each of these values by less than 0.5%.

The integral characteristics of the flow are in good agreement with the known data of other authors. Thus, for $\mathrm{Re} = 10^3$, $\mathrm{M} = 0.1$, $\mathrm{Pr} = 0.72$, our numerical result $\overline{C_D} = 1.511$, $\mathrm{St} = 0.2378$ differs by less than 0.3% from the values $(\overline{C_D} = 1.5092$, $\mathrm{St} = 0.2372)$, obtained by R.D. Henderson for incompressible flows [19, 20]. For $\mathrm{Re} = 100$, $\mathrm{M} = 0.4$, $\mathrm{Pr} = 0.72$, our numerical result $\overline{C_D} = 1.431$,
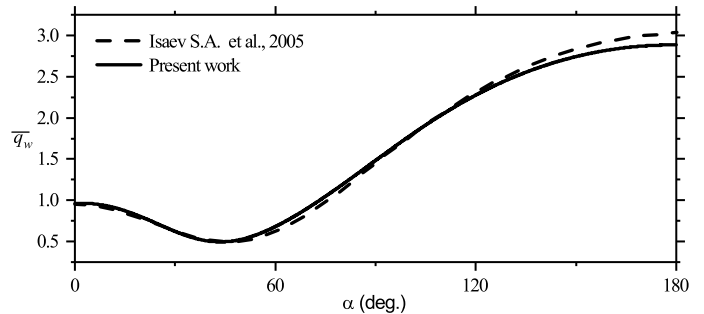

Fig. 1: Distribution of averaged heat flux $q_w = T_\infty^{-1}|\nabla T \cdot \boldsymbol{n}|$ over a heated cylinder for $\mathrm{Re} = 140$, $\mathrm{Pr} = 0.72$, $\mathrm{M} = 0.1$, the temperature of the cylinder is $1.273T_\infty$ (in this case, the boundary condition of constant cylinder wall temperature was specified); dashed line - calculations for incompressible flow from [22], solid line - present calculations.

$\triangle C_L = 0.333$, $\mathrm{St} = 0.1615$ differs by less than 2% from the data of [21] $(\overline{C_D} = 1.45$, $\triangle C_L = 0.328$, $\mathrm{St} = 0.162)$. The calculated distribution of averaged heat flux $q_w = T_\infty^{-1}|\nabla T \cdot \boldsymbol{n}|$ over a heated cylinder with constant temperature $1.273T_\infty$ (the condition of constant temperature of the cylinder wall was used only in this test case) for $\mathrm{Re} = 140$, $\mathrm{Pr} = 0.72$, $\mathrm{M} = 0.1$ is shown in Fig. 1. Our results are in good agreement with the incompressible-flow calculations from [22].

In the present study, the time-averaged parameters of periodic flows are calculated according to the trapezoidal rule. Two periods with approximately 40 nodes on each of them have been used (for a non-periodic regime at $\mathrm{M} = 0.6$, an interval containing 25 vortex shedding cycles was chosen for averaging).

3. Results

The next two subsections deal with two approaches to studying the energy separation process. At first (Section 3.1), we investigate the mechanisms of the total-enthalpy variation in fluid particles. Secondly (Section 3.2), the causes of energy redistribution in a time-averaged flow are studied. Basically, the analysis is carried out for the regime $\mathrm{Re} = 10^3$, $\mathrm{M} = 0.4$, $\mathrm{Pr} = 0.72$, the influence of Re, M, and Pr is considered in the last subsection (Section 3.2.3).

3.1. Total Enthalpy in a Fluid Particle

The energy separation effect in the wake behind the cylinder for $\mathrm{Re} = 10^3$, $\mathrm{M} = 0.4$, $\mathrm{Pr} = 0.72$ is illustrated in Fig. 2a-d, where, for four instants of time on half-period, we plotted the patterns of the normalized total enthalpy I_0 (in the following text the word 'normalized' is omitted when this does not lead to uncertainty):

$$I_0 = \frac{i_0 - i_{0\infty}}{i_{0\infty}}, \ i_0 = \gamma T + \frac{1}{2} U^2. \qquad (2)$$

Here,

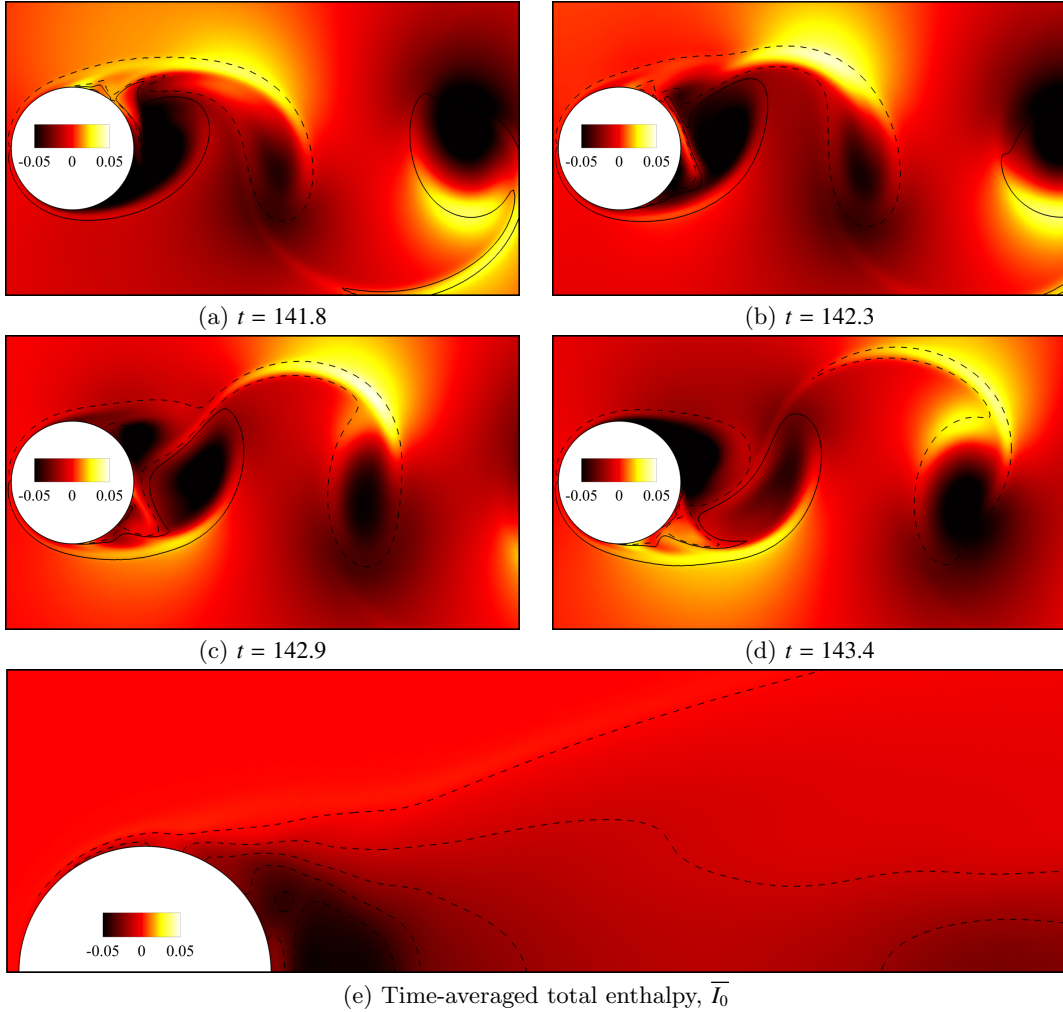$$i_{0\infty} = \frac{1}{(\gamma - 1)\mathrm{M}^2} + \frac{1}{2}$$

4

(a) $t = 141.8$

(b) $t = 142.3$

(c) $t = 142.9$

(d) $t = 143.4$

(e) Time-averaged total enthalpy, $\overline{I_0}$

Fig. 2: Energy separation effect in the wake behind the body: instantaneous (a-d) and time-averaged (e) total enthalpy I_0 at Re $= 10^3$, M $= 0.4$, Pr $= 0.72$. Solid and dashed lines on plots (a-d) are lines of $\omega = \pm$const; dashed lines on plot (e) are lines of $\overline{I_0} = $ const. At $t = 141.8$, the lift coefficient attains its minimum (the interval of the initial transients is $0 \leqslant t \lesssim 50$). Limit values on the color maps are not maximum and minimum of functions: function values greater than the upper limit (or less than the lower limit) are filled with one color corresponding to this limit.

is the dimensionless total enthalpy in the free stream, $U^2 = u^2 + v^2$. The total enthalpy i_0 differs from the total temperature (stagnation temperature) T_0 only by factor γ, and therefore the normalized total enthalpy I_0 is equal to the normalized total temperature.

Clearly, the regions of increased and reduced values of I_0 are concentrated near the vortices, with the gas portions characterized by negative values of I_0 always being located closer to the central part of the wake. After the time averaging of these flow patterns, we obtain that in the wake behind the cylinder near the symmetry axis there is a region of cooled gas ($I_0 < 0$) (see Fig. 2e). The most noticable reduction in I_0 is observed in the vortex formation region. This numerical demonstration of energy separation in the wake is consistent with the time-averaged [13] and time-resolved [11, 14] measurements of the wake flow.

We will now try to explain the reasons for the redistribution of I_0 in the flow. For doing this, it is convenient to write the equation of variation of the total enthalpy in the following form:

$$\frac{Di_0}{Dt} = \underbrace{\frac{1}{\rho}\frac{\partial p}{\partial t}}_{\mathcal{P}} + \underbrace{\frac{1}{\rho \text{Re}}\nabla \cdot (\boldsymbol{\tau} \cdot \boldsymbol{u})}_{\mathcal{A}} + \underbrace{\frac{1}{\rho \text{RePr}}\nabla^2 T}_{\mathcal{Q}}. \quad (3)$$

Here, $D/Dt = \partial/\partial t + \boldsymbol{u} \cdot \nabla$ is the material derivative. This equation follows from the energy conservation law for viscous heat-conducting gas. One can see that the variation of the stagnation enthalpy in a chosen fluid particle can be associated with the contribution of three terms on the right-hand side:

1. $\mathcal{P}$ is the specific pressure variation rate at a given point of space, which characterizes the change of the enthalpy due to the non-stationarity of the flow;

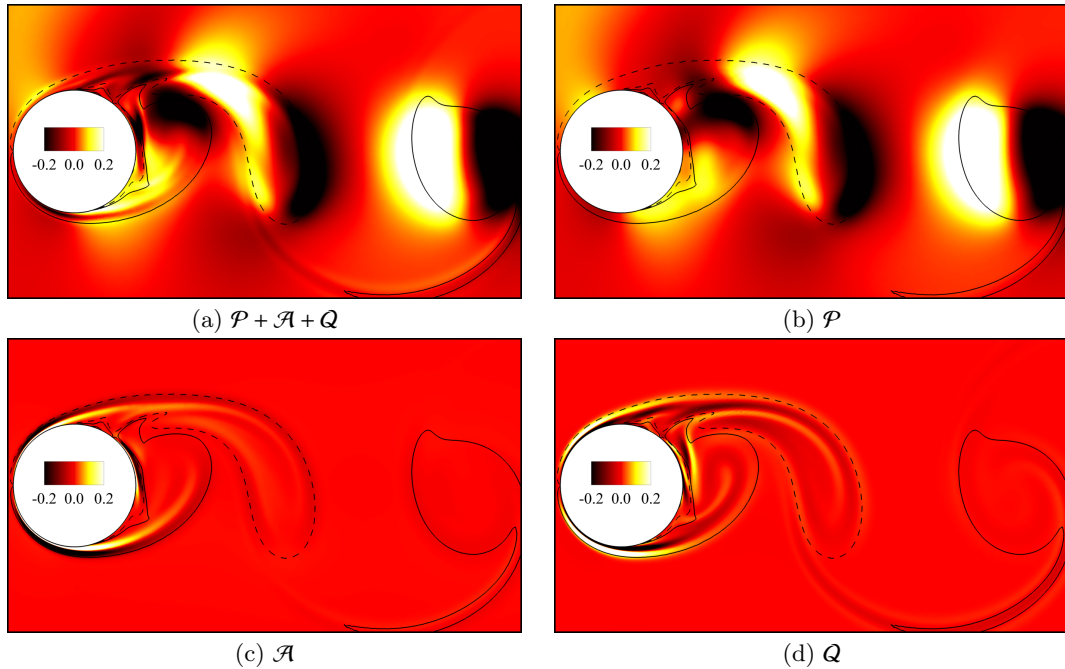2. $\mathcal{A}$ is the work of viscous forces per unit mass and unit time;

5

(a) $\mathcal{P} + \mathcal{A} + \mathcal{Q}$

(b) $\mathcal{P}$

(c) $\mathcal{A}$

(d) $\mathcal{Q}$

Fig. 3: The rate of variation of total enthalpy Di_0/Dt (a) in the fluid particle and the contribution of three mechanisms: $\mathcal{P}$ (b), $\mathcal{A}$ (c), $\mathcal{Q}$ (d) at Re = 10^3, M = 0.4, Pr = 0.72. Solid and dashed lines are lines of $\omega = \pm$const. The time instant corresponds to the minimum value of the lift coefficient, $t = 141.8$. Limit values on the color maps are not maximum and minimum of functions: function values greater than the upper limit (or less than the lower limit) are filled with one color corresponding to this limit.

3. $\mathcal{Q}$ is the heat release per unit mass and unit time due to the thermal conduction effect.

If the value of a term is positive (negative), than the corresponding mechanism tends to increase (decrease) the total enthalpy i_0 of a chosen fluid particle. By calculating the flow parameters, we can construct the fields of the values of different terms: $\mathcal{P}$, $\mathcal{A}$, $\mathcal{Q}$ (see Fig. 3).

As is clear from the patterns in Fig. 3, with the exception of a local flow region near the cylinder surface, the variation of i_0 in fluid particles is caused mainly by term $\mathcal{P}$. It follows from Eq. (3) that if the dissipative mechanisms are omitted than a redistribution of i_0 is possible only because of $\mathcal{P}$, which is associated with the variation of only the kinetic energy. Indeed, from the equations of variation of kinetic and internal energy

$$\frac{D}{Dt}\left(\frac{1}{2}U^2\right) = \frac{1}{\rho}\frac{\partial p}{\partial t} - \frac{D}{Dt}\left(\frac{p}{\rho}\right) + p\frac{D}{Dt}\left(\frac{1}{\rho}\right), \qquad (4)$$

$$\frac{De}{Dt} = -p\frac{D}{Dt}\left(\frac{1}{\rho}\right), \qquad (5)$$

it can be seen that the transitions between the internal and kinetic energy are described only by the third term in the first equation (the work of internal surface forces). Therefore, the term $\mathcal{P} = \rho^{-1}\partial p/\partial t$ (part of the work of external surface forces) is responsible only for a change of kinetic energy and can only indirectly affect the variation of internal energy.

In the vicinity of the rearmost point of the cylinder, the field $\mathcal{P}$ (Fig. 3b) is changed significantly after taking into account the contribution of $\mathcal{A} + \mathcal{Q}$ (Fig. 3a). Therefore, the contribution of the dissipative mechanisms is significant near the rearmost point and must be taken into account when explaining the Eckert–Weise effect. It is also clear from Fig. 4 which shows how the fields of I_0, Di_0/Dt, $\mathcal{P}$, and $\mathcal{A} + \mathcal{Q}$ on the cylinder surface depend on α, time t, and the position of the first separation point. In the rear part of the cylinder, both fields of $\mathcal{P}$ (Fig. 4c) and $\mathcal{A} + \mathcal{Q}$ (Fig. 4d) play an important role in the time variation of I_0 (Fig. 4a).

3.1.1. Laminar Boundary Layer

Ahead of the separation point, the unsteady behavior of I_0 is determined by both fields $\mathcal{P}$ and $\mathcal{A} + \mathcal{Q}$ (Fig. 4). However, the action of the pressure variation $\mathcal{P}$ is not responsible for the process of energy separation across the boundary layer, because the values of the pressure in fixed cross-sections of the boundary layer change only slightly (therefore, $p_{,t}$ does not change significantly). That is why $\mathcal{P}$ affects the global increase/decrease of profiles I_0 in time and probably changes I_0 along the boundary layer, but the redistribution of energy in the direction normal to the body surface is mainly determined by $\mathcal{A} + \mathcal{Q}$. Thus, the field of $\mathcal{A} + \mathcal{Q}$ generates non-uniformities in the total-enthalpy variation rate Di_0/Dt across the boundary layer and thereby determines the shape of these profiles.

For the part of the boundary layer located ahead of the separation regions, for Re = 10^3, M = 0.4, Pr = 0.72 we obtained a decrease in the average value of the total enthalpy near the cylinder surface (see Fig. 5). This occurs due to

6

a more intense (on average) heat efflux associated with heat conduction Q, as compared to the enthalpy growth due to the work of the viscous forces $\mathcal{A}$. With increase in the distance from the frontal stagnation point, this effect becomes more pronounced.

As is clear from Fig. 4, the sum $\mathcal{A} + Q$ does not always tend to reduce the value of I_0 along the boundary layer. In Fig. 4d, one can see that there are instants of time when $\mathcal{A} + Q > 0$ and $\mathcal{A} + Q < 0$. This behavior is associated with non-stationarity of flow separation. The increase in the pressure causes the separation point to move upstream, reducing the transverse velocity gradient and the external-flow velocity. The last two circumstances lead to smaller values of the friction-force work ($\mathcal{A}$) and less intense heat efflux (Q). Judging by the fact that $\mathcal{A} + Q$ becomes negative, the process of changing $\mathcal{A}$ turns out to be more intense. Similarly, a decrease in pressure leads to positive values of $\mathcal{A} + Q > 0$. Figures 4c, d show that when the pressure is close to the minimum value, $\mathcal{A} + Q$ reaches its maximum and vice versa, a minimum of $\mathcal{A} + Q$ is attained in the vicinity of the maximum value of the pressure.

It should also be noted that for each cross-section of the boundary layer there are such time instants when the value of I_0 is positive (see Fig. 5), i.e. the stagnation temperature T_0 on the surface is greater than the free-stream stagnation temperature. The maximum instantaneous value of T_0, attained behind the separation point (at $\alpha \approx \pm 100°$), is by 3% greater than the free-stream value of T_0.

3.1.2. Vortex Street

In [9], the following mechanism of energy redistribution in a vortex street was proposed. Inside the vortices, the pressure is smaller than outside; accordingly, when a fluid particle travels ahead of the vortex, we have $\mathcal{P} < 0$ (because $p_{,t} < 0$) and the enthalpy I_0 decreases; behind the vortex $\mathcal{P} > 0$ (because $p_{,t} < 0$) and the enthalpy I_0 increases. Below, we will confirm this explanation based on the calculation of the pattern of $DI_0/Dt = \mathcal{P} + \mathcal{A} + Q$ and the trajectories of chosen fluid particles.

Some examples of the calculated fluid-particle trajectories are shown in Fig. 6. The first four plots correspond to the patterns of I_0 in Fig. 2. Let us trace the motion of a particle marked by symbol $\diamond$. It travels along the curve similar to a cycloid around the vortex rotating in the clockwise direction. At the first three instants of time, the particle is located in the upstream part of the vortex, where $\mathcal{P} + \mathcal{A} + Q > 0$. Accordingly, I_0 increases and attains its local positive maximum approximately at a point of maximum distance from the axis of symmetry (Fig. 6c, i). Then, the fluid particle enters the leeward part of the vortex ($\mathcal{P} + \mathcal{A} + Q < 0$) and I_0 drops to its minimum value, attained on the opposite side of the vortex. A situation is possible in which the fluid particle is not 'trapped' by the vortex but is transported from one side of the vortex street to the other (see, for instance, the migration of symbol $\square$ in Fig. 6). In this case, when the fluid particle approaches the centerline it is affected by the upstream vortex, and

(a) I_0

(b) $\mathcal{P} + \mathcal{A} + Q$
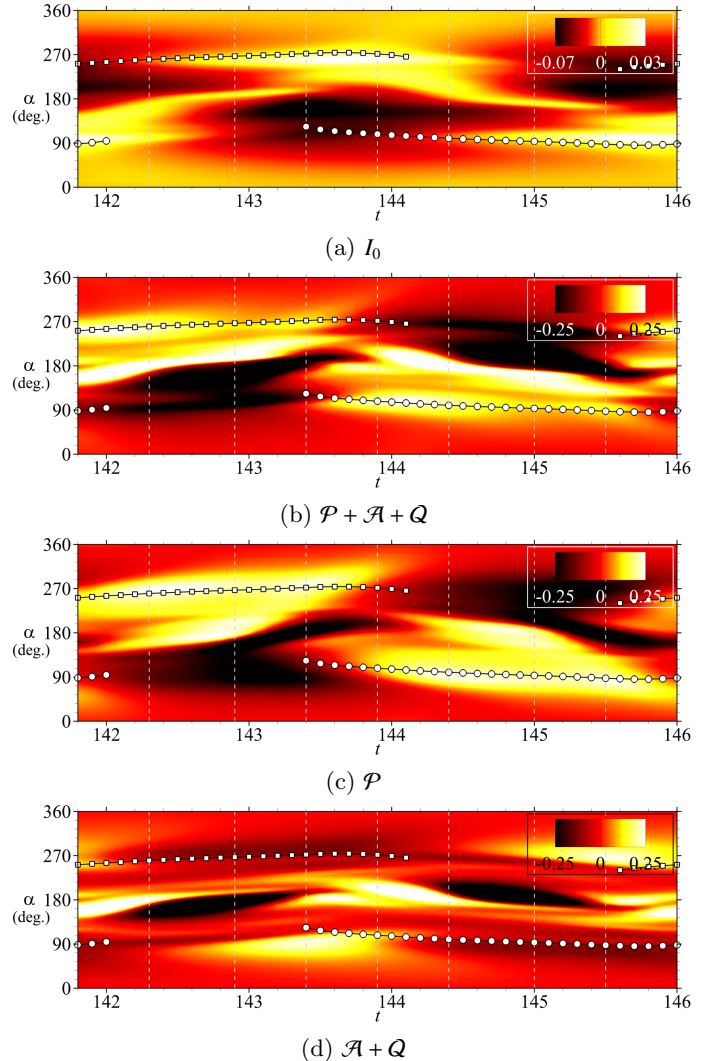
(c) $\mathcal{P}$

(d) $\mathcal{A} + Q$

Fig. 4: Variation of the total enthalpy on the surface (a) and the mechanisms responsible for this variation at $Re = 10^3$, $M = 0.4$, $Pr = 0.72$: $\mathcal{P} + \mathcal{A} + Q$ (b), $\mathcal{P}$ (c) and $\mathcal{A} + Q$ (d). Solid lines show the position of the separation point (the nearest to the frontal stagnation point for both sides of the cylinder), when it disappears the line breaks; dashed white lines mark the time instants corresponding to the plots in Fig. 6a-h. Limit values on the color maps are not maximum and minimum of functions: function values greater than the upper limit (or less than the lower limit) are filled with one color corresponding to this limit.

$\mathcal{P} + \mathcal{A} + Q < 0$, with the value of I_0 being decreased. After the particle crosses the centerline, I_0 begins to grow under the influence of the downstream vortex.

As is clear from Fig. 2, the growth of I_0 is also observed in the tail regions of the shed vortices. This again can be associated with mechanism $\mathcal{P}$ (see Fig. 3). In the region where the tail of the vortex is detached from the cylinder, the streamlines have a high curvature, so that at the instant of vortex shedding the pressure increases ($\mathcal{P} > 0$). Therefore, in the fluid particles moving in the direction outside the wake, the total enthalpy is increased, which can be seen in the regions near the vorticity tails (Fig. 2). These areas are transferred downstream. As the
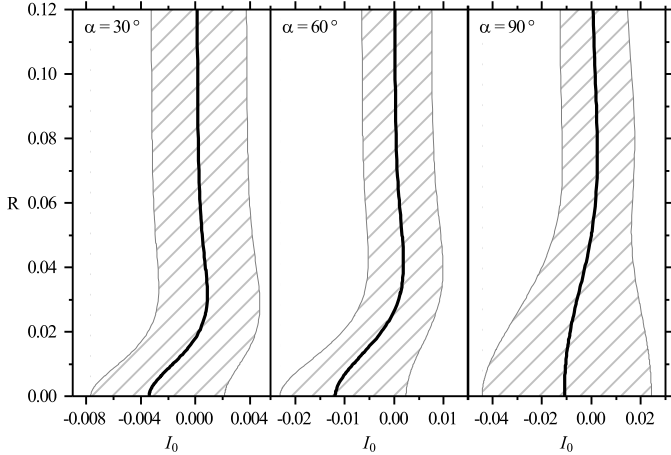
Fig. 5: Total enthalpy I_0 in boundary layer at $\alpha = 30°, 60°, 90°$, Re = 10^3, M = 0.4, Pr = 0.72. R is the distance from the cylinder surface. The shaded region shows the scatter of the values of I_0 on a period.

vortices are being shed from the cylinder, the curvature of the streamlines near their tails decreases, so the growth rate of I_0 due to the term $\mathcal{P}$ also decreases.

When a vortex street in the wake is absent, a region of reduced values of the total enthalpy I_0 still exists, but this reduction is associated with the flow in the boundary layer, where negative values of I_0 are attributable to the intense heat efflux. To illustrate this fact, in Fig. 7 we present the patterns of the total enthalpy I_0 and the sum $\mathcal{A} + Q$ for a steady-state flow at Re = 30, M = 0.4, Pr = 0.72. The value of I_0 in the fluid particle attains a minimum in the vicinity of the point $\alpha = 90°$, and then tends to zero, as the fluid particle travels downstream. Figure 7b shows that for $0° \leqslant \alpha \lesssim 90°$, the decrease in I_0 due to the heat flux Q is more intense, than the increase in I_0 due to the friction forces $\mathcal{A}$. On the other hand, at $\alpha \gtrsim 90°$ the second mechanism dominates, and I_0 increases. A similar effect was observed earlier in experiments [12] with a splitter plate behind the cylinder, which suppressed the vortex shedding. It was shown, that because of the boundary layer flow the energy separation is still observed, but its efficiency is much smaller.

As is clear from Fig. 6, at sufficiently large distances from the body in some fluid particles the value of i_0 is smaller than that in the free stream by more than 6% (symbol $\diamond$, $x \approx 3$, $t \approx 144$). However, the averaged i_0 differs from the free-stream value by less than 5% (Fig. 2). The minimum values are attained near the body: for $x > 1.1$, the average value of i_0 differs from the free-stream value by less than 3%. By analyzing the variation of i_0 in individual fluid particles of an unsteady flow, it is difficult to predict where the energy separation effect will be most pronounced. In the flow around the cylinder considered in this study, in the region where the time-averaged total enthalpy is minimal, the contribution of each of the three mechanisms is of the same order. The fluid-particle trajectories are too tangled (see for instance the pathline of

symbol $\circ$, Fig. 6), and the analysis becomes too laborious. Accordingly, to discuss the efficiency of energy separation, it is more convenient to consider time-averaged solutions.

3.2. Total Enthalpy in the Time-Averaged Flow

Each flow parameter can be represented as the sum of the time-averaged value and a fluctuation. We denote them by $\overline{(\cdot)}$ and $(\cdot)'$, for example, $\boldsymbol{u} = \overline{\boldsymbol{u}} + \boldsymbol{u}'$. In the next two subsections, we will consider two forms of the equation describing the variation of the averaged total enthalpy $\overline{i_0}$ with the aim to understand the major physical mechanisms of the time-averaged energy separation process.

3.2.1. Approach 1 (Based on the Averaged Equation of Total-Enthalpy Evolution)

After the time averaging of the total enthalpy evolution equation (3), we obtain:

$$\overline{\boldsymbol{u}} \cdot \nabla \overline{i_0} = -\overline{\boldsymbol{u}' \cdot \nabla i_0'} + \underbrace{\overline{\frac{1}{\rho} \frac{\partial p}{\partial t}}}_{\overline{\mathcal{P}}} + \underbrace{\frac{1}{\text{Re}} \overline{\frac{1}{\rho} \nabla \cdot (\boldsymbol{\tau} \cdot \boldsymbol{u})}}_{\overline{\mathcal{A}}} + \underbrace{\frac{1}{\text{RePr}} \overline{\frac{1}{\rho} \nabla^2 T}}_{\overline{Q}}. \quad (6)$$

This equation gives the information about the variation of $\overline{i_0}$ along the averaged streamlines. In an unsteady flow, the term $-\overline{\boldsymbol{u}' \cdot \nabla i_0'}$ arises, which affects the average distribution of i_0. Thus, even if the sum of other mechanisms gives zero contribution, the time-averaged energy separation is still possible. The following example demonstrates this nonlinear effect.

It is convenient to consider a model one-dimensional advection equation with a source term:

$$i_{0,t} + u i_{0,x} = \mathcal{F}. \quad (7)$$

Here, all functions depend on x and t. Consider the following periodic solution of this equation:

$$i_0 = I(x)(1 - \frac{2}{a} \cos \nu t), \quad u = U(x)(1 + a \cos \nu t), \quad (8)$$

corresponding to a given function $\mathcal{F}$ with the mean value $\overline{\mathcal{F}} = 0$:

$$\mathcal{F} = \frac{2\nu}{a} I \sin \nu t - U I_{,x} \left[\left(\frac{2}{a} - a \right) \cos \nu t + \cos 2\nu t \right]. \quad (9)$$

Here, $I(x)$ and $U(x)$ are arbitrary functions, and $\nu \neq 0$ and $a \neq 0$ are arbitrary coefficients. For this solution, the mean values of $\overline{i_0}$ and $\overline{u}$ are equal to $I(x)$ and $U(x)$, and the variation of i_0 is caused by the presence of term $\mathcal{F}$: if $\mathcal{F} \equiv 0$, then $I(x) \equiv 0$.

In spite of the fact that the mechanism $\mathcal{F}$ is described by a periodic function with $\overline{\mathcal{F}} = 0$, the time-averaged value of the total enthalpy may decrease in the fluid particle, as it travels downstream. For example, let $a = 0.5$, $\nu = 2\pi$, $U(x) = 1$, $I(x) = -x$. Then we have:

$$\overline{u i_{0,x}} = -\overline{u' i'_{,x}} + \overline{\mathcal{F}} = -1. \quad (10)$$
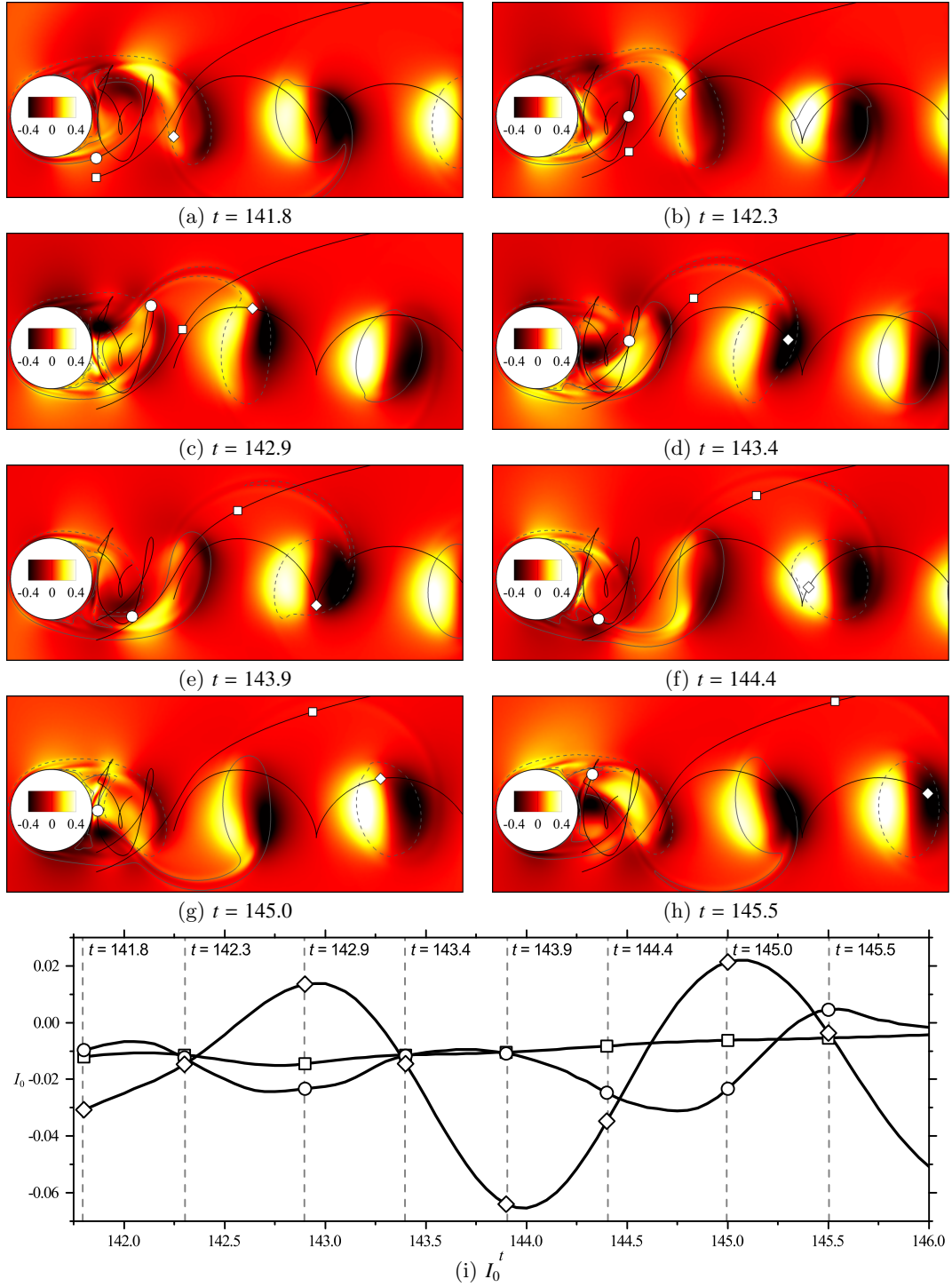
8

Fig. 6: The rate of variation of the total enthalpy DI_0/Dt in fluid particles for Re $= 10^3$, M $= 0.4$, Pr $= 0.72$: the patterns of DI_0/Dt and the pathlines of fluid particles for eight instants of time on the period (a-h). Plot (i) shows the dependencies $I_0(t)$ for each fluid particle. Gray solid and dashed lines in plots (a-d) are isolines $\omega = \pm$const. Black lines in plots (a-d) show the trajectories, and the symbols show the locations of liquid particles. The symbols correspond to those in plot (i). At $t = 141.8$, the lift coefficient attains its minimum. Limit values on the color maps are not maximum and minimum of functions: function values greater than the upper limit (or less than the lower limit) are filled with one color corresponding to this limit.
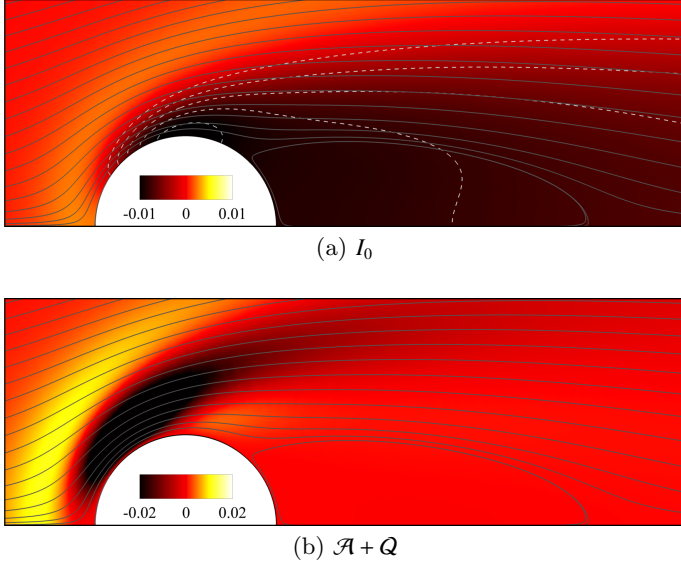
(a) I_0

(b) $\mathcal{A} + \mathcal{Q}$

Fig. 7: Energy separation for $\mathcal{P} = 0$ (the flow is steady-state), Re = 30, M = 0.4, and Pr = 0.72. The upper plot (a) shows the pattern of I_0 and the lower plot (b) the pattern of $\mathcal{A} + \mathcal{Q}$. Solid lines are streamlines; dashed lines in plot (a) are isolines $\overline{I_0}$ = const

This example clearly demonstrates that one cannot estimate the contribution of a specific mechanism to the energy separation process using only the time-averaged value of the term associated with this mechanism. The indirect effect associated with the term $-\overline{\boldsymbol{u}' \cdot \nabla i_0'}$ may be also important. If the non-stationary action of the source $\mathcal{F}$ ensures a positive correlation $\overline{(u - \overline{u})(i_{0,x} - \overline{i}_{0,x})}$ at the point of space, then $\overline{i}_0$ decreases along the flow direction.

When such nondimensionalization is used that the Mach number stands in the equations rather than in the boundary conditions, in Eq. (6) the factor M^{-2} appears in the term $\overline{\mathcal{P}}$. In Section 3.2.3 it will be shown that, in the regimes considered, the energy separation efficiency varies mainly with the Mach number. This is why the appearance of the negative correlation $\overline{\boldsymbol{u}' \cdot \nabla i_0'}$ in the wake is attributable to the action of the term $\overline{\mathcal{P}}$.

Figure 8a-e illustrates the time-averaged energy separation process for Re = 10^3, M = 0.4, Pr = 0.72. Figure 8a-b shows the total enthalpy $\overline{I_0}$ and the value of $\overline{\boldsymbol{u}} \cdot \nabla \overline{i}_0 / |\overline{\boldsymbol{u}}|$, characterizing the growth and decrease of $\overline{I_0}$ along the direction of the averaged streamlines. Using this data, a scheme illustrating the energy separation process was constructed (Fig. 9). There are three key regions (*Regions I, II, III* in the figure), which cause a decrease in the total enthalpy $\overline{i}_0$.

Region I is associated with the total-enthalpy decrease in the laminar boundary layer. Behind the body, the flow region can be separated by the streamlines bypassing the recirculation zones (bold lines in Fig. 9). Then the decrease in the total enthalpy near the rear part of the body is determined by *Region II*, and the values of $\overline{i}_0$ downstream are determined by the flow in the strip where $\overline{\boldsymbol{u}} \cdot \nabla \overline{i}_0 / |\overline{\boldsymbol{u}}| < 0$ (*Region III*), which provides negative values

for $\overline{I_0}$ in the wake.

The term $-\overline{\boldsymbol{u}' \cdot \nabla i_0'}$ makes the main contribution to the rate of variation of the total enthalpy in the averaged flow (Fig. 8c-e). It is clear that in the wake the sum $\overline{\mathcal{P}} + \overline{\mathcal{A}} + \overline{\mathcal{Q}}$ (Fig. 8e) is small as compared to $-\overline{\boldsymbol{u}' \cdot \nabla i_0'}$ (Fig. 8d), and the fields of $-\overline{\boldsymbol{u}' \cdot \nabla i_0'}$ and $\overline{\boldsymbol{u}} \cdot \nabla \overline{i}_0$ differ only slightly. Thus, in this interpretation, the mechanism of energy separation associated with the correlation $\overline{\boldsymbol{u}' \cdot \nabla i_0'}$ dominates in the wake. However, the reduction of $\overline{I_0}$ in the boundary layer is ensured mainly by $\overline{\mathcal{P}} + \overline{\mathcal{A}} + \overline{\mathcal{Q}}$ (more precisely, by the action of $\overline{\mathcal{Q}}$), which is dominant inside this region.

In the next section, using another form of equation for the averaged total enthalpy, we will present a more detailed information on the mechanisms that cause the change in the total enthalpy in *Regions I, II*, and *III*.

3.2.2. Approach 2 (Based on the Kinetic-Energy Equation)

From the law of conservation of momentum one can obtain the relation

$$\nabla i_0 = \nabla e - \boldsymbol{u}_{,t} + p\nabla \frac{1}{\rho} - \boldsymbol{\omega} \times \boldsymbol{u} + \frac{1}{\text{Re}} \frac{1}{\rho} \nabla \cdot \boldsymbol{\tau}. \qquad (11)$$

Here, $\boldsymbol{\omega} = (\nabla \times \boldsymbol{u})$ is the vorticity vector. The time-averaging and multiplication by the average value of the velocity lead to the following expression

$$\overline{\boldsymbol{u}} \cdot \nabla \overline{i}_0 = \overline{\boldsymbol{u}} \cdot \nabla \overline{e} + \overline{p \overline{\boldsymbol{u}} \cdot \nabla \frac{1}{\rho}} + \overline{\boldsymbol{\omega} \cdot (\overline{\boldsymbol{u}} \times \boldsymbol{u})} + \frac{1}{\text{Re}} \overline{\frac{1}{\rho} \overline{\boldsymbol{u}} \cdot (\nabla \cdot \boldsymbol{\tau})}. \quad (12)$$

The *first* and *second term* on the right-hand side of Eq. (12) relates the non-uniformity of the total enthalpy with the non-uniformities of the internal energy (or temperature) and the density along the averaged streamlines. The non-uniformity of $\overline{e}$ and $\overline{\rho}$ across the averaged flow direction does not contribute to a change in the total enthalpy (along the averaged streamlines). The *third term* results in either increase or decrease in $\overline{i}_0$ due to the change in the direction of instantaneous streamlines. The velocity fluctuations along the averaged flow direction do not contribute to a change in the total enthalpy. The *fourth term* expresses the influence of viscous forces on the energy redistribution.

For an incompressible inviscid and non-heat-conducting flow, the internal energy and density are constant in the entire flow field (when the free stream is uniform). Therefore, the first two and the fourth terms do not affect the distribution of $\overline{i}_0$. However, energy separation is still possible because of the third term. It should be noted that in the case of strictly incompressible flow the redistribution of $\overline{i}_0$ is in fact the redistribution of total pressure. If the flow is also irrotational or the streamlines do not vary in time (that is, $\boldsymbol{\omega} \cdot (\overline{\boldsymbol{u}} \times \boldsymbol{u}) = 0$), then the total enthalpy in the entire flow region is the same, and there can be no energy separation.

Let us now analyze the flow at Re = 10^3, M = 0.4, Pr = 0.72 based on this approach. Comparing the fields for
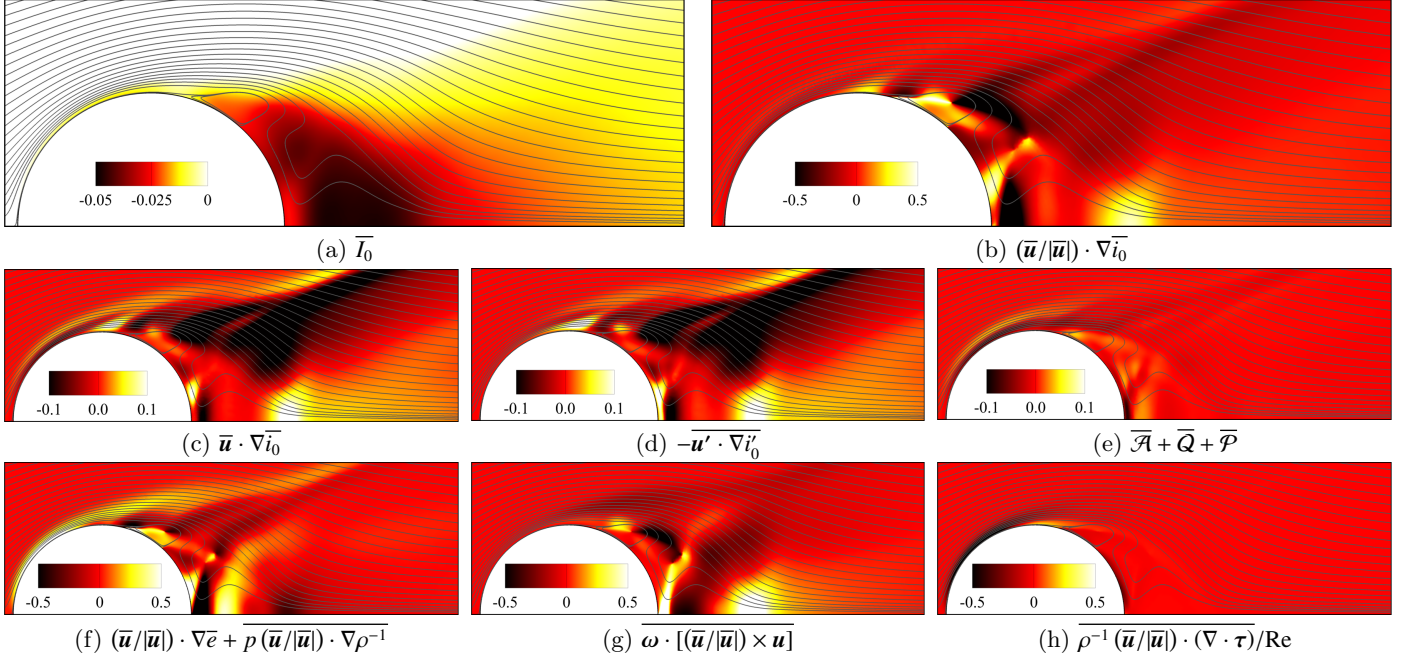
Fig. 8: Estimate of the terms in averaged Eqs. (6) and (12) for Re = 10^3, M = 0.4, Pr = 0.72. Solid lines show the streamlines. Limit values on the color maps are not maximum and minimum of functions: function values greater than the upper limit (or less than the lower limit) are filled with one color corresponding to this limit.
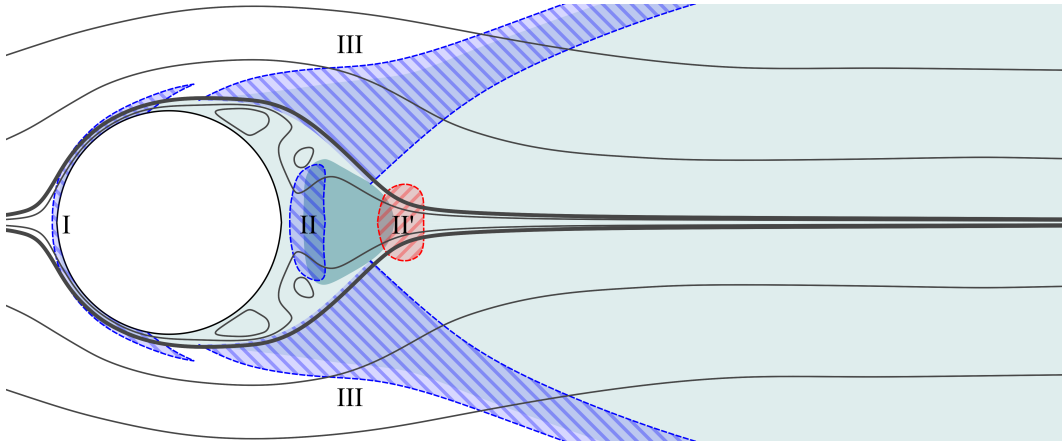
(a) $\overline{I_0}$

(b) $(\overline{\boldsymbol{u}}/|\overline{\boldsymbol{u}}|) \cdot \nabla \overline{i_0}$

(c) $\overline{\boldsymbol{u}} \cdot \nabla \overline{i_0}$

(d) $-\overline{\boldsymbol{u}' \cdot \nabla i_0'}$

(e) $\overline{\mathcal{A}} + \overline{\mathcal{Q}} + \overline{\mathcal{P}}$

(f) $(\overline{\boldsymbol{u}}/|\overline{\boldsymbol{u}}|) \cdot \nabla \overline{e} + \overline{p\,(\overline{\boldsymbol{u}}/|\overline{\boldsymbol{u}}|) \cdot \nabla \rho^{-1}}$

(g) $\overline{\boldsymbol{\omega} \cdot [(\overline{\boldsymbol{u}}/|\overline{\boldsymbol{u}}|) \times \boldsymbol{u}]}$

(h) $\overline{\rho^{-1}\,(\overline{\boldsymbol{u}}/|\overline{\boldsymbol{u}}|) \cdot (\nabla \cdot \boldsymbol{\tau})}/\mathrm{Re}$

Fig. 9: Scheme of energy separation in the time-averaged flow. In *Regions I-III*, $\overline{I_0}$ is decreased and in *Region II'* $\overline{I_0}$ is increased. The shaded region in the wake shows where $\overline{I_0} < 0$. The flow in the wake is divided in two parts by bold streamlines, with the decrease in $\overline{I_0}$ in each part being mostly described by the flow through one of *Regions II, III*.

the contribution of each mechanism (Fig. 8f-h) with their total-action field (Fig. 8b), we will obtain information on the role of each mechanism in the formation of *Regions I, II, III* (Fig. 9).

Region I provides a decrease in the total enthalpy in the laminar boundary layer and is primarily related to the action of the fourth term in Eq. (12). The work of friction forces (Fig. 8h) most strongly affects the flow in the boundary layer and gives a negative contribution to the rate of change in the total enthalpy for $|\alpha| \lesssim 80°$ (behind the separation point, $80° \lesssim |\alpha| \lesssim 105°$, friction forces act in the opposite way).

The constructed energy separation scheme in the wake

(Fig. 9) shows that a cold spot near the body is associated with the vortex formation process (*Region II*), and the decrease in i_0 in the wake is associated with the flow in the tails of detached vortices (*Region III*).

The strongest decrease in $\overline{I_0}$ in *Region II* is associated with the contribution of the first three terms in Eq. (12). The sum of the first two terms act, in general, opposite to the third term (Fig. 8f, g). The comparison of the fields related to the total action of all mechanisms (Fig. 8b) and the field associated with the action of only the term $\overline{\boldsymbol{\omega} \cdot (\overline{\boldsymbol{u}} \times \boldsymbol{u})}$ (Fig. 8g) shows that behind the cylinder the qualitative behaviour of $\overline{I_0}$ can be described mainly by the third mechanism (changing the direction of the stream-

11
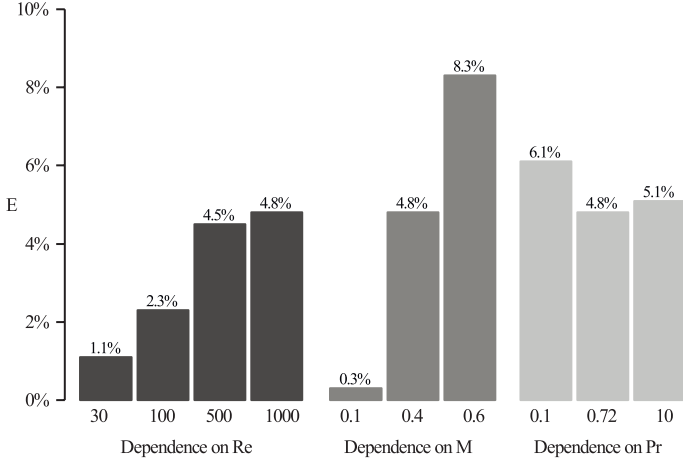
Fig. 10: Efficiency of energy separation at various Reynolds (M = 0.4, Pr = 0.72), Mach (Re = 10^3, Pr = 0.72) and Prandtl (Re = 10^3, M = 0.4) numbers.

lines), and the sum of the first two mechanisms (Fig. 8f) only weakens this effect. The third term affects the field of $\overline{I_0}$ in two ways: on one hand, it causes the reduction of $\overline{I_0}$ behind the body in *Region II*, and on the other hand it leads to an increase in $\overline{I_0}$ downstream in *Region II′*. As a result, a minimum value of $\overline{I_0}$ is attained near the body surface.

Regarding the Eckert–Weise effect, from the comparison of the fields in Fig. 8 one can see that near the cylinder surface the gas is cooled because of the fourth term in Eq. (12) at the frontal part of the cylinder (Fig. 8h) and because of non-uniformities in the temperature and density fields at the rear part of the cylinder (first two terms in Eq. (12), Fig. 8f). This allows to conclude that the effect of reduction of $\overline{I_0}$ in the rear part of the cylinder is associated with the non-uniformity of temperature and density created by the evolution of recirculation zones near the body surface.

Region III is the strip where $\overline{\boldsymbol{u}} \cdot \nabla \overline{i_0}/|\overline{\boldsymbol{u}}| < 0$, extending into the wake (Fig. 8b). This region is a result of the action of the first three terms in Eq. (12). Due to the flow in this region, a zone of reduced average total enthalpy in the wake is created. The location of this strip in space is determined by the position of the tails of the vortices detached from the body (Fig. 2). In the region $y > 0$ ($y < 0$), the tails with $\omega < 0$ ($\omega > 0$) are formed and then travel away from the symmetry line. This means that the vectors $\overline{\boldsymbol{u}} \times \boldsymbol{u}$ and $\boldsymbol{\omega}$ are oriented in opposite directions, so that $\boldsymbol{\omega} \cdot (\overline{\boldsymbol{u}} \times \boldsymbol{u}) < 0$, and the $\overline{I_0}$ decreases. A non-uniformity in the internal energy and density in *Region III* tends to increase $\overline{I_0}$ on one part of this region and to reduce it on the other part. However, it turns out that on the whole for this flow regime these mechanisms make a smaller contribution to the rate of change of the total enthalpy as compared with the action of the third term.

It should be noted that at Re = 30 (Fig. 7) the flow region in the wake also has a reduced temperature, although the third term on the right-hand side of Eq. (12) is identi-

cally equal to zero (the flow is stationary, hence $\overline{\boldsymbol{u}} = \boldsymbol{u}$ and $\overline{\boldsymbol{u}} \times \boldsymbol{u} = 0$). In this case, a strip similar to that shown in the figure also exists (Fig. 7b), but the decrease of I_0 in this region is determined by the work of the friction forces. This strip corresponds to *Region I*, which at Re = 30 extends downstream, rather than ends at $\alpha \approx \pm 90°$, as for Re = 10^3. Thus, depending on the values of the dimensionless parameters, the degree of influence of different mechanisms and the energy redistribution scheme can change, thereby changing the efficiency of energy separation. In the next section, we discuss the efficiency of energy separation for different flow regimes.

3.2.3. Efficiency of the Energy Separation

Let the efficiency of energy separation E be described by the minimal value in the field of the normalized time-averaged total enthalpy $E = |min(\overline{I_0})|$. This quantity indicates the difference of the minimal value of the averaged total enthalpy i_0 from $i_{0\infty}$. Figure 10 shows the values of E for different regimes.

Influence of the Reynolds number Re. As Re increases from 30 to 10^3, E increases in more than 4 times. However, the difference between the value of E for Re = 500 and Re = 10^3 is only 0.3%. The main influence of the increase in the Reynolds number on the energy separation process is associated with the intensification of the vortex shedding process. As a result, the strongest changes in $\overline{I_0}$ occur in *Regions II, II′* and *III*. Except for the case of Re = 30, the minimum of $\overline{I_0}$ is attained at a certain distance from the body (see Fig. 2, Fig. 11a, d). At Re = 30, the minimum of $\overline{I_0}$ is attained at the points $\alpha = \pm 89°$ on the surface of the cylinder (Fig. 7).

The character of the distribution of $\overline{I_0}$ over the body surface also varies significantly, depending on the value of Re (Fig. 12a). The positions and the number of extrema of $\overline{I_0}$ are determined by the dynamics and number of separation zones in the rear part of the body. The behavior of $\overline{I_0}$ in the boundary layer region turns out to be similar for different Re, since both the terms responsible for the friction forces ($\mathcal{A}$) (which results in the increase of $\overline{I_0}$) and for the heat conduction ($\mathcal{Q}$) (which results in the decrease of $\overline{I_0}$) contain the same factor $1/Re$.

At the frontal stagnation point $x = -0.5$, $y = 0$ the value of $\overline{I_0}$ is not strictly equal to 0 (Fig. 12a), which is due to the viscosity and thermal conductivity effects in the vicinity of this point. Consider a steady-state flow along the x-axis in a narrow stream tube on the symmetry axis. Simplifying the expressions on the right-hand side of Eq. (3), we obtain that on the surface with the outward normal $(0, 1)$ the variation of i_0 can be caused by the viscous forces $u_y u/(\rho Re)$ and thermal conductivity $T_y/(\rho Re Pr)$. In the problem considered, near the line $y = 0$ we always have a reduction in the value of u and increase in temperature T. Accordingly, the work o f the viscous forces always increases I_0, and the heat efflux leads to a decrease in I_0. This is why in Fig. 12a the increase in Re results in approaching $\overline{I_0}$ to
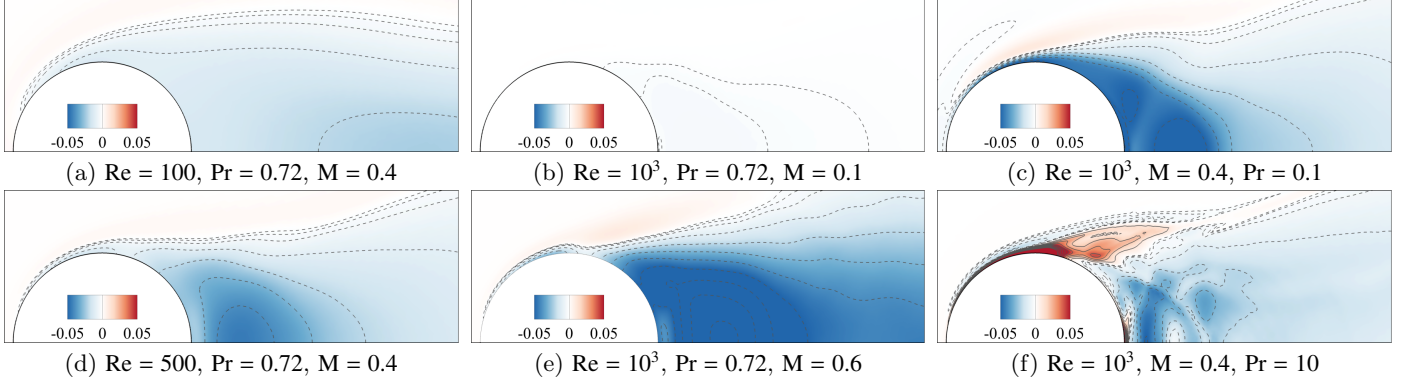
Fig. 11: Influence of Re (a, d), M (b, e), Pr (c, f) on time-averaged total enthalpy $\overline{I_0}$. Solid and dashed lines are lines of $\overline{I_0}$ = const. Limit values on the color maps are not maximum and minimum of functions: function values greater than the upper limit (or less than the lower limit) are filled with one color corresponding to this limit. Actually, in the depicted flow region the value of $\overline{I_0}$ varies within the limits: $(-0.0229, 0.0023)$ (a); $(-0.0034, 0.0002)$ (b); $(-0.0609, 0.0099)$ (c); $(-0.0447, 0.0027)$ (d); $(-0.0833, 0.0089)$ (e); $(-0.0511, 0.2059)$ (f).
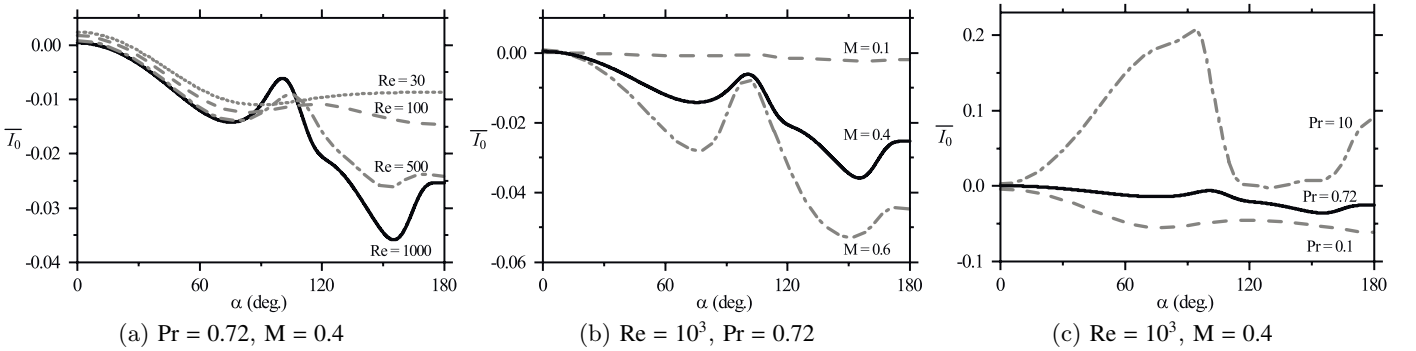
Fig. 12: Time-averaged total enthalpy $\overline{I_0}$ distribution on the cylinder surface at various values of Re, M and Pr.

0 at the point $x = -0.5$, $y = 0$, while a decrease in Pr enhances the negative contribution of heat conduction to the value of i_0, which results in the decrease in $\overline{I_0}$ below zero at Pr = 0.1 (Fig. 12c).

Influence of the Mach number M. The increase in the Mach number from M = 0.1 to M = 0.6 results in a more then 25-fold increase in E (Fig. 10, Fig. 11b, e). If we use such nondimensionalization that the Mach number enters in the equations, rather than in the boundary conditions, the factor M^{-2} appears in the first two terms of Eq. (12). Noting that the contribution of the sum of these terms in *Region II* is opposite to that of the third term (Fig. 8b), we can assume that this is why the increase in the Mach number should lead to an increase in the efficiency of energy separation. This agrees with the assumption that the third term in Eq. (12), related to the unsteadiness of streamlines, is the key mechanism causing the reduction of the total enthalpy in the wake.

Influence of the Prandtl number Pr. A variation of the Prandtl number affects significantly the surface distribution of the parameters (Fig. 12c), changes the pattern of $\overline{I_0}$ near the cylinder (Fig. 11c, f), but surprisingly has a relatively slight impact on the energy separation efficiency E (see Fig. 10). For instance, the increase in Pr from 0.72

to 10 results in a growth of I_0 on the whole (Fig. 11f) and near the separation point the value of i_0 becomes approximately by 20% greater than in the free stream (Fig. 12c). However, in the wake near the rear part of the cylinder the minimal value of $\overline{I_0}$ slightly differs from the corresponding value for Pr = 0.72 (Fig. 10). Thus, despite the impact of heat conductivity has been reduced by more than on order of magnitude, we still have the similar effect of energy separation. For Pr = 0.1, the minimum is located on the body at the point $\alpha = 180°$, but the cold region in the wake still exists and has the similar structure.

It should be noted that all conclusions made in this subsection are based on only a qualitative consideration, because the mechanisms do not change independently with the change of Re, M, and Pr.

4. Conclusion

From our numerical simulations, we can draw the following conclusions.

- A non-uniformity in the total-enthalpy distribution across the boundary layer in unsteady flow is attributable to the action of dissipative mechanisms.

13

- In the vortex street, the process of total-enthalpy variation in fluid particles is associated with pressure fluctuations and is well described by the model proposed in [9].

- To describe the strongest decrease in the averaged total enthalpy in the vortex formation region and the Eckert–Weise effect, it is necessary to take into account the action of all dissipative and non-stationary mechanisms: viscous forces, thermal conductivity, and part of the work of the external surface forces, associated with pressure fluctuations at the points of space.

- The total-enthalpy stratification in the time-averaged flow can be associated mainly with the action of the mechanism described by the term $\overline{\boldsymbol{u}' \cdot \nabla i_0'}$, which arises after averaging the nonlinear convective derivative. However, the appearance of a negative correlation $\overline{\boldsymbol{u}' \cdot \nabla i_0'}$ in the wake is attributable to the action of the term $\mathcal{P}$ (pressure variation rate at a given point of space).

- The estimate of the main factors affecting the averaged flow (Fig. 8) indicates the following.
    - The Eckert–Weise effect is associated mainly with non-uniformities in the temperature and density fields, created by the evolution of recirculation zones near the body surface.
    - In the wake, the time-averaged total enthalpy decreases mainly due to streamline oscillations.

- Three characteristic regions of reduced total enthalpy i_0 can be distinguished in the flow (Fig. 9). *Region I* is associated with the decrease in $\overline{i_0}$ in the boundary layer. *Regions II* and *III* determine the decrease in $\overline{i_0}$ in the wake behind the body. Moreover, the averaged flow in the wake can be divided into two parts, so that *Regions II* and *III* determine the decrease in $\overline{i_0}$ in different parts of the wake (Fig. 9). *Region II*, located in the vortex formation zone, is responsible for the appearance of minimal values of $\overline{i_0}$ near the body surface. *Region III* is a strip along which the tails of the shed vortices travel; this region is responsible for lowering of $\overline{i_0}$ in the wake behind the vortex formation region. Thus, it was obtained that the decrease in $\overline{i_0}$ in this part of the wake (in the developed vortex street) is caused by the motion of vortex tails.

Acknowledgement

Appendix A. The Navier–Stokes equations in primitive variables

The matrices in Eq. (1) take the following form:

$$A_0 = \frac{1}{(\gamma-1)T} \begin{pmatrix} 1 & 0 & 0 & -\frac{p}{T} \\ u & p & 0 & -\frac{pu}{T} \\ v & 0 & p & -\frac{pv}{T} \\ \varepsilon & pu & pv & -\frac{pU^2}{2T} \end{pmatrix},$$

$$A_1 = \frac{1}{(\gamma-1)T} \begin{pmatrix} u & p & 0 & -\frac{pu}{T} \\ u^2 & 2pu & 0 & -\frac{pu^2}{T} \\ uv & pv & pu & -\frac{puv}{T} \\ u\varepsilon & pu^2+p\varepsilon & puv & -\frac{puU^2}{2T} \end{pmatrix},$$

$$A_2 = \frac{1}{(\gamma-1)T} \begin{pmatrix} v & 0 & p & -\frac{pv}{T} \\ uv & pv & pu & -\frac{puv}{T} \\ v^2 & 0 & 2pv & -\frac{pv^2}{T} \\ v\varepsilon & puv & pv^2+p\varepsilon & -\frac{pvU^2}{2T} \end{pmatrix},$$

$$K_{11} = \begin{pmatrix} 0 & 0 & 0 & 0 \\ 0 & \frac{4}{3\mathrm{Re}} & 0 & 0 \\ 0 & 0 & \frac{1}{\mathrm{Re}} & 0 \\ 0 & \frac{4u}{3\mathrm{Re}} & \frac{v}{\mathrm{Re}} & \frac{\gamma}{\mathrm{Pr}\mathrm{Re}} \end{pmatrix}, K_{12} = \begin{pmatrix} 0 & 0 & 0 & 0 \\ 0 & 0 & -\frac{2}{3\mathrm{Re}} & 0 \\ 0 & \frac{1}{\mathrm{Re}} & 0 & 0 \\ 0 & \frac{v}{\mathrm{Re}} & -\frac{2u}{3\mathrm{Re}} & 0 \end{pmatrix},$$

$$K_{21} = \begin{pmatrix} 0 & 0 & 0 & 0 \\ 0 & 0 & \frac{1}{\mathrm{Re}} & 0 \\ 0 & -\frac{2}{3\mathrm{Re}} & 0 & 0 \\ 0 & -\frac{2v}{3\mathrm{Re}} & \frac{u}{\mathrm{Re}} & 0 \end{pmatrix}, K_{22} = \begin{pmatrix} 0 & 0 & 0 & 0 \\ 0 & \frac{1}{\mathrm{Re}} & 0 & 0 \\ 0 & 0 & \frac{4}{3\mathrm{Re}} & 0 \\ 0 & \frac{u}{\mathrm{Re}} & \frac{4v}{3\mathrm{Re}} & \frac{\gamma}{\mathrm{Pr}\mathrm{Re}} \end{pmatrix},$$

$$\boldsymbol{P}_1 = p\,(0,1,0,u)^*, \quad \boldsymbol{P}_2 = p\,(0,0,1,v)^*.$$

Here, $\varepsilon = T + U^2/2$.

References

[1] G. J. Ranque, Expériences sur la détente giratoire avec productions simultanées d'un échappement d'air chaud et d'un échappement d'air froid, J. Phys. Radium 4 (7) (1933) 112–114.

[2] S. Eiamsa-ard, P. Promvonge, Review of Ranque–Hilsch effects in vortex tubes, Renewable and sustainable energy reviews 12 (7) (2008) 1822–1842. doi:10.1016/j.rser.2007.03.006.

[3] A. I. Leont'ev, Gas–dynamic method of energy separation of gas flows, High Temperature 35 (1) (1997) 155–157.

[4] A. I. Leontiev, A. G. Zditovets, Y. A. Vinogradov, M. M. Strongin, N. A. Kiselev, Experimental investigation of the machine-free method of temperature separation of air flows based on the energy separation effect in a compressible boundary layer, Experimental Thermal and Fluid Science 88 (2017) 202–219. doi:10.1016/j.expthermflusci.2017.05.021.

[5] G. M. Azanov, A. N. Osiptsov, The efficiency of one method of machineless gasdynamic temperature stratification in a gas flow, International Journal of Heat and Mass Transfer 106 (2016) 1125–1133. doi:https://doi.org/10.1016/j.ijheatmasstransfer.2016.10.090.

[6] E. Eckert, W. Weise, Messungen der Temperaturverteilung auf der Oberfläche schnell angeströmter unbeheizter Körper, Forschung im Ingenieurwesen 13 (6) (1942) 246–254. doi:10.1007/BF02585343.

[7] L. F. Ryan, Experiments on aerodynamic cooling, Ph.D. thesis, Swiss Federal Institute of Technology, Zurich (1951). doi:10.3929/ethz-a-000092033.

[8] H. Thomann, Measurements of the recovery temperature in the wake of a cylinder and of a wedge at mach numbers between 0.5 and 3, National Aeronautical Research Institute (FFA), Sweden, Report 84 (1959).

[9] M. Kurosaka, J. B. Gertz, J. E. Graham, J. R. Goodman, P. Sundaram, W. C. Riner, H. Kuroda, W. L. Hankey, Energy separation in a vortex street, Journal of Fluid Mechanics 178 (1987) 1–29. doi:10.1017/S0022112087001095.

[10] E. R. G. Eckert, Cross transport of energy in fluid streams, Wärme-und Stoffübertragung 21 (2-3) (1987) 73–81. doi:10.1007/BF01377562.

[11] W. F. Ng, W. M. Chakroun, M. Kurosaka, Time-resolved measurements of total temperature and pressure in the vortex street behind a cylinder, Physics of Fluids A 2 (6) (1990) 971–978. doi:10.1063/1.857604.

[12] R. J. Goldstein, B. He, Energy separation and acoustic interaction in flow across a circular cylinder, Journal of Heat Transfer 123 (4) (2001) 682–687. doi:10.1115/1.1378020.

[13] R. J. Goldstein, K. S. Kulkarni, Energy Separation in the Wake of a Cylinder, Journal of Heat Transfer 130 (6) (2008) 061703–061703–9. doi:10.1115/1.2891222.

[14] J. Ackerman, J. Gostelow, A. Rona, W. Carscallen, Energy separation and base pressure in the wake of a circular cylinder, in: 32nd AIAA Fluid Dynamics Conference and Exhibit, Fluid Dynamics and Co-located Conferences, American Institute of Aeronautics and Astronautics, 2002, pp. 1–10. doi:10.2514/6.2002-3302.

[15] T. J. R. Hughes, G. Scovazzi, T. E. Tezduyar, Stabilized Methods for Compressible Flows, Journal of Scientific Computing 43 (3) (2010) 343–368. doi:10.1007/s10915-008-9233-5.

[16] A. I. Aleksyuk, V. P. Shkadova, V. Y. Shkadov, Formation, evolution, and decay of a vortex street in the wake of a streamlined body, Moscow University Mechanics Bulletin 67 (3) (2012) 53–61. doi:10.3103/S0027133012030016.

[17] A. I. Aleksyuk, Investigation of the separated flows by the numerical solution of Navier–Stokes equations, Ph.D. thesis, M.V. Lomonosov Moscow State University (2013).

[18] A. I. Aleksyuk, V. P. Shkadova, V. Y. Shkadov, Numerical simulation of three-dimensional instability of flow past a short cylinder, Moscow University Mechanics Bulletin 71 (1) (2016) 1–6. doi:10.3103/S0027133016010015.

[19] R. D. Henderson, Details of the drag curve near the onset of vortex shedding, Physics of Fluids 7 (9) (1995) 2102–2104. doi:10.1063/1.868459.

[20] C.-Y. Wen, C.-Y. Lin, Two-dimensional vortex shedding of a circular cylinder, Physics of Fluids 13 (3) (2001) 557–560. doi:10.1063/1.1338544.

[21] D. Canuto, K. Taira, Two-dimensional compressible viscous flow around a circular cylinder, Journal of Fluid Mechanics 785 (2015) 349–371. doi:10.1017/jfm.2015.635.

[22] S. A. Isaev, A. I. Leontiev, N. A. Kudryavtsev, T. A. Baranova, D. A. Lysenko, Numerical simulation of unsteady-state heat transfer under conditions of laminar transverse flow past a circular cylinder, High Temperature 43 (5) (2005) 746–759. doi:10.1007/s10740-005-0119-z.